NeuroImage 298 (2024) 120758

Contents lists available at ScienceDirect

NeuroImage

journal homepage: www.elsevier.com/locate/ynimg

CalciSeg: A versatile approach for unsupervised segmentation of calcium imaging data

Yannick Günzel [a,b,c,d,*], Einat Couzin-Fuchs [b,c,d], Marco Paoli [e,**]

[a] International Max Planck Research School for Quantitative Behaviour, Ecology and Evolution from lab to field, 78464 Konstanz, Germany
[b] Department of Biology, University of Konstanz, 78464 Konstanz, Germany
[c] Department of Collective Behavior, Max Planck Institute of Animal Behavior, 78464 Konstanz, Germany
[d] Centre for the Advanced Study of Collective Behaviour, University of Konstanz, 78464 Konstanz, Germany
[e] Neuroscience Paris-Seine – Institut de biologie Paris-Seine, Sorbonne Université, INSERM, CNRS, 75005 Paris, France

ARTICLE INFO

Dataset link: www.github.com/YannickGuenzel/CalciSeg/, www.doi.org/10.5281/zenodo.8403062

Keywords:
Calcium imaging
Image segmentation
Source extraction
Antennal lobe
Insect

ABSTRACT

Recent advances in calcium imaging, including the development of fast and sensitive genetically encoded indicators, high-resolution camera chips for wide-field imaging, and resonant scanning mirrors in laser scanning microscopy, have notably improved the temporal and spatial resolution of functional imaging analysis. Nonetheless, the variability of imaging approaches and brain structures challenges the development of versatile and reliable segmentation methods. Standard techniques, such as manual selection of regions of interest or machine learning solutions, often fall short due to either user bias, non-transferability among systems, or computational demand. To overcome these issues, we developed *CalciSeg*, a data-driven and reproducible approach for unsupervised functional calcium imaging data segmentation. *CalciSeg* addresses the challenges associated with brain structure variability and user bias by offering a computationally efficient solution for automatic image segmentation based on two parameters: regions' size limits and number of refinement iterations. We evaluated *CalciSeg* efficacy on datasets of varied complexity, different insect species (locusts, bees, and cockroaches), and imaging systems (wide-field, confocal, and multiphoton), showing the robustness and generality of our approach. Finally, the user-friendly nature and open-source availability of *CalciSeg* facilitate the integration of this algorithm into existing analysis pipelines.

1. Introduction

Functional calcium imaging has become a standard method for the study of neuronal circuits due to the ability to monitor large neural ensembles *in vivo* over extended periods of time (Kerr and Denk, 2008). Following the fluorescent activity of genetically encoded calcium indicators (Miyawaki et al., 1997; Chen et al., 2013) and organic dyes (Tsien, 1980), it provides an indirect yet reliable readout of neuronal activity (Denk et al., 1996; Jayaraman and Laurent, 2007; Hires et al., 2008), and can be applied at a wide range of spatial and temporal scales: from single boutons (Bilz et al., 2020) to whole brain measurements (Ahrens et al., 2013), and from high-resolution recordings over a few seconds (Paoli et al., 2024) to measurements in freely-behaving animals over multiple days (Wirtshafter and Disterhoft, 2022).

Calcium activity can be captured via different microscopy systems, including wide-field, confocal, and multiphoton microscopy. While wide-field microscopy is more cost-effective, it is limited by lower spatial resolution and reduced depth penetration. In contrast, confocal and two-photon microscopy are more expensive laser-scanning techniques that offer higher axial resolution. Two-photon microscopy specifically utilizes infrared light to induce a fluorescent transition, making it less phototoxic and intrinsically capable of higher penetration. Despite using different recording approaches — field recording with a CCD/CMOS camera in the case of fluorescent imaging, pixel scanning, and reconstruction in the case of laser-scanning microscopes — all methods converge on the production of 3-D time-lapse images, where the first two dimensions define the field of view (x and y) and the third one is time (t).

Automated data-driven analysis allows for an unbiased interpretation of functional imaging data. However, despite significant progress in prediction tools, machine learning, and high-dimensional statistics, functional imaging analysis still relies heavily on manual processing. A major challenge is accurately identifying the regions of interest (ROIs),

* Corresponding author at: Department of Biology, University of Konstanz, 78464 Konstanz, Germany.
** Corresponding author.
E-mail addresses: yannick.guenzel@uni-konstanz.de (Y. Günzel), mar.paoli@gmail.com (M. Paoli).

https://doi.org/10.1016/j.neuroimage.2024.120758
Received 29 April 2024; Received in revised form 30 April 2024; Accepted 25 July 2024
Available online 31 July 2024

which can refer to individual neurons or functional units in the imaging area. When the target tissue is relatively homogenous, *i.e.* containing cell bodies that are similar in size and shape, automatic detection has become more prevalent (reviewed by Abbas and Masip (2022)). Various computational approaches have been used for cell body detection, including correlation-based clustering (Pachitariu et al., 2016; Spaen et al., 2019), independent component analysis (ICA, Mukamel et al. (2009)), non-negative matrix factorization (NNMF, Giovannucci et al. (2019)) and deep convolutional neural network segmentation (Stringer et al., 2021; Sità et al., 2022; Islam et al., 2023).

Conversely, identifying functional units that are heterogeneous in size and shape remains challenging for any segmentation algorithm. This is also compounded by the large volume of data generated in such experiments and by variability in quality between trials and within a single measurement. Despite the importance of automatic ROI-detection for ensuring an unbiased and reproducible extraction of relevant functional units (Pnevmatikakis, 2019; Abbas and Masip, 2022), this process is often considered computationally intensive or challenging to implement. Theoretically, such a process searches for temporally correlated features without prior information on their structure and dynamics. This can be done via the analysis of the covariance matrix across all pixels within the imaging window followed by either independent component analysis (ICA) or Promax oblique rotation, allowing for grouping of temporally correlated pixels (Mölter et al., 2018). In a recent study, Münch and colleagues performed an extensive functional analysis of the gustatory processing center of the fruit fly — the sub-esophageal zone — to investigate gustatory coding and the influence of the internal state on food choice (Münch et al., 2022). They used ICA to extract spatial features from the measured activity along a 4-D imaging stack and created a functional atlas of this brain area. Spatial ICA is a data-driven method largely used for the analysis of functional magnetic resonance imaging (fMRI) data and provides the possibility to identify sets of mutually correlated brain regions without prior information on their temporal dynamics (Varoquaux et al., 2010).

Calcium imaging analysis has a central role in the study of olfactory coding. In insects, the first olfactory processing center is the antennal lobe (AL), a globular neuropil analogous to the vertebrate olfactory bulb (Wilson and Mainen, 2006). The AL consists of structural and functional units, the olfactory glomeruli, that process input from the olfactory sensory neurons (OSNs) and relay the resulting information to higher-order brain centers via multiple projection neuron (PN) tracts. Each glomerulus is innervated by the OSNs expressing the same olfactory receptor. Consequently, an odorant interacting with a particular subset of olfactory receptors will activate a distinct subset of glomeruli. This generates an odorant-specific response map within the glomerular population (Galizia et al., 1999b) that represents information on the odorant's chemical properties (Sachse et al., 1999) and concentration (Sachse and Galizia, 2003). The direct correspondence between a stimulus and the encoded response is a fundamental aspect of the logic of odor coding, a mechanism that is shared across vertebrate and invertebrate species. The number of glomeruli is generally conserved within a species but may vary drastically across animals. Among insects, their number ranges from approx. 50 glomeruli in the fly (Hallem and Carlson, 2004), 165 in the bee (Galizia et al., 1999a), 205 in the American cockroach (Watanabe et al., 2010), and more than 1000 in the desert locust (Anton and Hansson, 1996; Hansson et al., 1996). Additionally, they can vary in size with relatively large glomeruli in the honey bee (approx. 50 μm in diameter; Arnold et al. (1985)) and microglomeruli in the locust (approx. 10 μm; Anton and Hansson (1996)).

Antennal lobe calcium imaging analysis provides an exciting case for developing algorithms for segmenting functionally relevant regions. Understanding the neurophysiology of olfactory coding and perception requires the study of odorant-induced activity across the glomerular space, a task that hinges on the reliable segmentation of glomeruli across stimuli, individuals, and experimental conditions. Still, constructing a robust ROI-detecting algorithm remains challenging, given the large variability in the number and shape of glomeruli across imaging sessions and insect species. In some cases, such as the honey bee or the fruit fly ALs, the anatomical definition of glomerular units allows for accurate manual labeling, providing a clear ground truth image for developing a segmentation algorithm.

Current solutions for glomerular detection rely on dimensionality reduction approaches for detecting the spatial components describing response variability across the glomerular space. For instance, Reidl and colleagues were able to analyze odorant responses in the mouse olfactory bulb using spatial independent component analysis (ICA) (Reidl et al., 2007). Similarly, Strauch and Galizia adopted a principal component analysis (PCA) to extract the spatial features describing stimulus distribution in the fly (Strauch and Galizia, 2011) and the bee AL (Strauch et al., 2013). Using their prior knowledge of the dataset, they selected a subset of biologically relevant pixels to be included in the PCA, thus improving processing time. Alternative methods employ regularized non-negative matrix factorization, which allows incorporating the user's knowledge of the dataset to enhance the quality of segmentation, *e.g.*, glomerular size, and relative location (Soelter et al., 2014).

Here, we introduce *CalciSeg*, an open-source pipeline for functional imaging data segmentation (Fig. 1). Specifically, the local extremes in the time-collapsed intensity projection of a 3-D dataset provide the seeds for a Voronoi tessellation, which divides the projection into regions comprising all pixels closer to that extreme than to the neighboring ones. This operation is followed by an optional phase of iterative segmentation refinements based on time course similarity (Fig. 1B). Our method provides a fully unsupervised, data-driven, and reproducible solution for calcium imaging data segmentation and functional unit extraction that can efficiently be run on a commercial desktop computer or laptop. Moreover, it can be applied to datasets of different complexity and comprising ROIs of different sizes and shapes.

2. Material and methods

2.1. *CalciSeg*: Calcium imaging data segmentation

In the following subsections, we outline the sequential steps undertaken by *CalciSeg* to segment spatial regions exhibiting coherent temporal patterns in a functional imaging dataset (Fig. 1).

2.1.1. Data input and pre-processing

CalciSeg processes functional imaging data organized in a 3-D matrix with dimensions x, y, and t, where x and y represent the sides of the imaging field, and t the temporal dimension of the video, *i.e.*, the number of frames. Hence, video files from imaging sessions exported in tiff or any proprietary format should be opened and loaded into MATLAB (MathWorks Inc, Natick, MA, USA) as a 3-D matrix to be processed by *CalciSeg*. *CalciSeg* requires no additional metadata, such as spatial or temporal resolution details, simplifying the pre-processing phase and making the tool accessible to a broad range of users.

2.1.2. Temporal intensity projections

Commonly, calcium imaging data are summarized as 2-D visualizations by applying a summary statistic that flattens the temporal dimension of the data. The key features of such a time-collapsed intensity projection form the basis of the initial segmentation employed by *CalciSeg*, and each projection method offers a unique view of the data, influencing the subsequent analysis. Thus, it is essential to understand the nuances of each approach to choose the most appropriate projection method.

The maximum (*max*) and minimum (*min*) intensity projections capture each pixel's highest or lowest values over time, respectively, to identify regions of extreme activity. These projection methods result

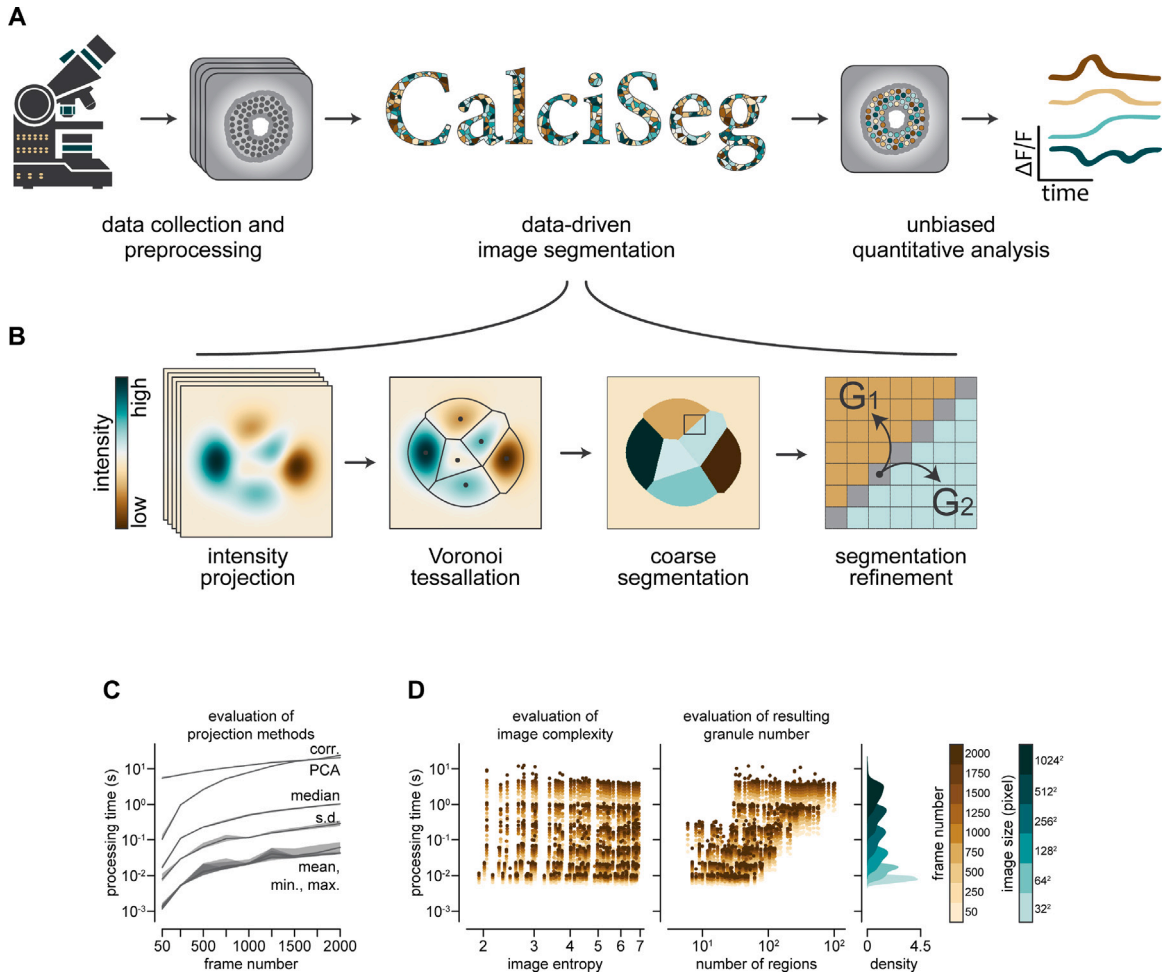

Fig. 1. Efficient data-driven segmentation of calcium imaging data. **(A)** Typical imaging pipeline with *CalciSeg* as a central aspect for an unbiased quantitative analysis of calcium imaging data. **(B)** Functionality of *CalciSeg*, which applies a Voronoi tessellation on the dataset's intensity projection to obtain a first segmentation of the data. The segmentation can be further refined through an iterative process that evaluates pixels along the borders between two granules (*e.g.*, $G1$ and G_2). **(C)** Some projection methods are faster than others. For all, the processing time increases with frame number. Image size is 256 × 256 pixels. **(D)** Processing time remains unaffected by image complexity but increases with image size. Individual maximum intensity projections for the mock datasets differing in image complexity are shown in suppl. Fig. 1.

in clear and sharp images. However, they overemphasize brief events and do not offer information about the variability or consistency of the data.

The mean intensity projection (*mean*) captures each pixel's average behavior over time. This can be particularly useful for getting a clear representation of the data by diluting transient noise or anomalies, emphasizing regions with stable and consistent activity. However, this projection method is prone to outliers and a potential loss of detail.

Similarly, the median intensity projection (*median*) captures each pixel's average behavior over time but with a representation resistant to outliers. Thus, it offers a more robust central tendency and a compromise between the mean intensity projection and max/min projection (see above). However, this projection method is computationally more expensive than the mean intensity projection and comes with a potential loss of extremes.

The standard deviation projection (*std*) captures each pixel's variability in intensity over time. It can be instrumental in identifying regions of activity, emphasizing rare or transient events that might be missed with other projection methods. However, this projection method is prone to noise and lacks information on the absolute intensity.

A principal component analysis can reduce the temporal dimensionality of the data. The strongest component can be used as a projection (*pca*) that captures the primary modes of variation in the data. However, as the primary source of variation in imaging time series is often change in amplitude, this method provides similar information to the mean or median intensity projection while being computationally more expensive.

Last, a local correlation map (*corr*) can be used as a projection method. This method calculates how strongly each pixel correlates with the average time course of its immediate neighbors (Pearson's linear correlation coefficient). The neighbors are identified via a disk-shaped structuring element with a radius (r) based on the minimum pixel count (*mincount*, first entry to the input variable *limitPixCount*) per region ($r = \lceil \sqrt{mincount/\pi} \rceil$). In the case of *limitPixCount* being set to *auto*, the radius is set to one. This approach offers valuable insight into the local divergence of the data. However, note that evaluating each pixel's neighborhood is time-consuming, and processing time is expected to increase with increases in both the number of pixels and the number of frames.

Notably, computing the mean, maximum, and minimum intensity projections is computationally efficient, and the number of frames in a calcium imaging experiment does not substantially impact processing time. On the other hand, projection methods based on PCA or pixel correlation are more complex and, as a result, are heavily influenced by the number of frames and, as a general rule, about 100-fold slower. Projections based on standard deviation or median fall somewhere in between (Fig. 2A). In these cases, processing time can be improved by reducing the temporal domain of the data through PCA-pre-processing or manual frame selection before initiating the *CalciSeg* processing pipeline.

2.1.3. Image segmentation

The core functionality of *CalciSeg* is the reliable and reproducible segmentation of a calcium imaging time series into distinct "activity granules" (terminology inspired by solar granulation, *c.f.* Spruit et al., 1990). To this end, *CalciSeg* defines local seeds by identifying regional maxima and minima within the intensity projection. Such local extremes are defined as the centroids of connected sets of pixels with a constant intensity value, surrounded by pixels with lower (for local maximum) or higher (local minimum) values. The local neighborhood is based on the 3×3 area surrounding each pixel (adjacent pixels in the horizontal, vertical, and diagonal directions). Next, *CalciSeg* uses such seeds to group pixels of the projection image based on their Voronoi topology. In other words, each pixel is associated with its nearest seed, resulting in a Voronoi tessellation that remains consistent across different runs due to the deterministic nature of Delaunay triangulation.

The process of identifying regional seeds can be further fine-tuned by the input variable *regmax_method*. This parameter specifies whether the intensity projection image should be used without any changes (*regmax_method* = *raw*), whether it should be smoothed (*regmax_method* = *filtered*), or whether the seeds from both approaches should be combined (*regmax_method* = *both*). To smooth the intensity projection and emphasize local extreme values, we applied moving minimum and maximum filters through morphological operations (dilating/eroding the image for max./min. filtering, respectively). These operations are conducted via a disk-shaped structuring element with a radius (r) based on the minimum pixel count (*mincount*, first entry to the input variable *limitPixCount*) per region ($r = \lceil \sqrt{mincount/\pi} \rceil$).

2.1.4. Advanced refinement processes

Following the initial segmentation via Voronoi tessellation (Fig. 1B), *CalciSeg* initiates a refinement stage aimed at the identification of functional units of biologically plausible size and shape. This step engages an iterative process that consists of evaluating whether the temporal profile of pixels at the intersection between neighboring granules is more akin to one or the other. In essence, the time series data TS for each pixel p, situated at the intersection of the granules (G_1 and G_2), is compared against the average time series data of the respective regions (TS_{G1} and TS_{G2}). Based on the resulting score, pixel p is assigned to the granule with the more similar activity profile. This similarity assessment can be carried out in two different ways, specified by input variable *refinement_method*: using a correlation operation (*refinement_method* = *corr*) or by calculating the root median square error (*refinement_method* = *rmse*) between TS_p and the centroids TS_{G1} and TS_{G1}. This operation is performed iteratively until either the maximum number of iterations (*n_rep*) or an optimal solution is reached. Note that the refinement is based on a pairwise vector comparison, which increases with vector length, *i.e.*, the number of frames.

Concurrently, *CalciSeg* monitors granule sizes before the refinement and during each iteration, redistributing pixels from excessively small granules to adjacent regions or dividing oversized granules. The adjustment of oversized granules was achieved via a watershed transform to segment them into smaller units or, if this fails, we applied a division along the granule's principal axes. Additionally, if refinement leads to a granule being segmented into separate regions, *e.g.*, through "pinching off" a subregion, these new subregions are assigned a new ID. Thus, taken together, the number and shape of granules can change substantially throughout the refinement process. Yet, each step being deterministic allows for a reproducible segmentation result, provided that the number of refinement iterations remains constant.

2.1.5. Output

The main output of *CalciSeg*, *granules_labeled*, is a mask with the regions' IDs. This mask is a matrix in the same spatial dimensions, x and y, as the input stack. The second output, *summary_stats*, is a MATLAB structure containing the intensity projection image (*projection*), each granule's average time course (*avgTCs*; rows: granules, columns: time steps), each granule's average within-pixel correlation (*granule_Corr*), the binned mean intensity projection (*granule_Avg_img*), the binned minimum intensity projection (*granule_Min_img*), the binned maximum intensity projection (*granule_Max_img*), the binned standard deviation projection (*granule_Std_img*), and a binary image based on the intensity projection used for segmentation, indicating which granules were active. Active granules are determined by applying Otsu's method (Otsu, 1979).

2.1.6. MATLAB dependencies

CalciSeg was developed in MATLAB and tested using version R2023a. The project relies on several toolboxes that must be installed before use. The required toolboxes and their applications are Image Processing Toolbox, Statistics and Machine Learning Toolbox, and Parallel Computing Toolbox.

2.2. Alternative segmentation approaches

The number of image segmentation approaches for functional imaging data has increased substantially in the past few years (reviewed by Abbas and Masip (2022)). To benefit from the overall simple-to-use architecture of the *CaciSeg* implementation and provide potential users with the possibility to compare other approaches to our new one, we compared the efficiency and efficacy of *CalciSeg* to two common methods for unsupervised segmentation: a region-growing approach and an approach based on independent component analysis.

2.2.1. Correlation-based region-growing

One approach for the segmentation of (irregular) spatiotemporal regions is a region-growing algorithm grouping pixels in correlation space (*e.g.*, Zhu and Yuille (1996) and Spaen et al. (2019)). Since one of the projection methods offered by *CalciSeg* is estimating the dataset's correlation space (*projection_method* = *corr*), we also provide a region-growing approach for comparison with the Voronoi tesselation (*init_seg_method* = *corr*). Note that this method relies on an additional arbitrary threshold (cutoff correlation coefficient for stopping the growing phase). In addition, estimating the dataset's correlation space is considerably slower than any of the other intensity projections (Fig. 1), and growth time is likely to be substantially affected by image size and frame number. In our implementation of the region-growing method, seeds are pixels with an average correlation coefficient of $r > 0.85$ with their neighborhood. The first seed is the pixel with the highest r value. Neighboring pixels that are above the threshold are gradually added to the pixel's cluster until the maximum number of pixels is reached or no neighboring pixel is above the threshold anymore.

2.2.2. Reconstruction independent component analysis

Another approach is a workflow based on an independent component analysis (ICA) to extract regions of interest (*e.g.*, Beckmann and Smith (2004), Münch et al. (2022), Aimon et al. (2019) and Weiser et al. (2023)). In our implementation of this method, first, we subtracted the mean time course from the data, then, we performed a pre-whitening step based on singular value decomposition (SVD). This operation transforms the data so that it has zero mean and identity covariance, essentially cropping noise components. This is important as mean signal effects in the data render source separation impossible for ICA. Finally, we applied a principal component analysis before a complete feature extraction using reconstruction ICA (Matlab in-built *rica* function). Due to the statistical properties of the data, the mean of the negative side of a component can be larger than the mean of the positive side (and vice versa). Here, the sign was chosen so that the mean of the negative side of the component is always smaller. Hence, in the end, pixels are segmented based on the component with the most substantial effect while accounting for split regions.

2.3. Mock data for benchmark testing

We created mock datasets with varying numbers of pixels, frames, and regions to evaluate the performance of *CalciSeg* and the different intensity projection methods. For this, we gradually increased the image size of $2^n \times 2^n$ pixels with n gradually increasing from 5 to 10. We tested each image size with an increasing number of frames starting with 50, 250, and then in steps of 250 until 2000 frames. In addition, we evaluated different levels of image complexity by varying the number of regions in the image (suppl. Fig. 1). Last, to obtain the time courses over a given number of frames, we multiplied each pixel's value with a region-specific stream of uniformly distributed random numbers and smoothed the stack with 3-D Gaussian filtering (s.d. of 8). Overall, we tested ten repetitions of all 324 different combinations of pixel number (6 levels), frame number (9 levels), and image complexity (6 levels), measuring the segmentation time using the MATLAB stopwatch timer. The *CalciSeg* parameters used for the segmentation are listed in Table 1.

2.4. Exemplary data: Functional multiphoton imaging in Apis mellifera

Experiments were performed on honey bees reared in outdoor hives on the campus of the University of Paul Sabatier (Toulouse, France; see Paoli et al. (2024) for details). Honey bee foragers were collected the day before the experiment at an artificial feeder, to which they were previously trained, and projection neurons were labeled for calcium imaging analysis with 10 kDa dextran-conjugated Fura-2 (Thermo Fisher Scientific, Waltham, MA, USA) as previously described (Paoli et al., 2017; Sachse and Galizia, 2002). After dye injection, bees were fed with 50% water/sugar solution and kept overnight in the dark and at room temperature. On the following day, the antennal lobe (AL) was exposed and labeled individuals were subjected to calcium imaging analysis during olfactory stimulation. Undiluted solutions of 1-hexanol, 1-heptanol, and peppermint oil (Sigma-Aldrich) were loaded onto the olfactory stimulator and delivered to the bees at a 10^{-1} dilution using an Arduino Uno®-controlled automated olfactometer (Raiser et al., 2017; Bestea et al., 2022). Odorants were alternated and presented 20 times on a 5/25 s ON/OFF configuration.

Calcium imaging recordings were conducted with a straight Leica SP8 scanning microscope (Leica Microsystems, Germany) equipped with a SpectraPhysics InSight X3 multiphoton laser tuned at 780 nm for Fura-2 excitation. All images were acquired with a water immersion 16x objective (Leica HC FLUOTAR 16x/0.6 IMM CORR, Leica Microsystems, Germany) at 64 × 64 pixel resolution and 127 frames per second. Calcium imaging data were pre-processed with custom-made MATLAB scripts. The baseline signal, calculated as the mean fluorescence during the one second before stimulus onset, was used to calculate baseline-subtracted and normalized stimulus-induced glomerular activity ($\Delta F/F_0$). The normalized activity was multiplied by −1 to display excitatory/inhibitory responses as positive/negative relative changes ($-\Delta F/F_0$).

2.5. Exemplary data: Functional confocal imaging in Schistocerca gregaria

Following a recently established protocol, we conducted calcium imaging of the olfactory projection neurons (PNs) of gregarious adult desert locusts (Petelski et al., 2024). Antennal lobe PNs were retrogradely labeled with a dextran-conjugated calcium indicator (Cal-520-Dextran Conjugate MW 10,000; Biomol, Hamburg, Germany) by localized dye injection into the medial calyx of the mushroom bodies. The dye was allowed to travel overnight by placing the labelled and restrained animals in a humid chamber at 15 °C. For functional imaging, antennae were gently relocated ventrally, exposing the ALs, and the imaging site was sealed with translucent silicone (Kwik-Sil; World Precision Instruments; Sarasota, FL, USA). Calcium imaging was conducted at a laser-scanning confocal microscope (LSM 510; Carl Zeiss Microscopy, Oberkochen, Germany) equipped with a water immersion objective (W Plan-Apochromat 20×/1,0 DIC VIS-IR; Carl Zeiss Microscopy).

Functional data was acquired with a resolution of 256 × 256 pixel at 1 frame per second from two imaging depths. First, from a layer approximately 35 µm beneath the surface of the AL to acquire data from PN cell bodies. Then, from a deeper layer (approximately 135 µm beneath the AL surface) to capture glomerular responses. Odor stimuli, cis-3-hexenyl-acetate (diluted to 10^{-2} in mineral oil), 1-hexanol (diluted to 10^{-3}), and 3-octanol (diluted to 10^{-2}) (Sigma-Aldrich, Steinheim, Germany), were delivered to the locusts using a custom-built olfactometer (Raiser et al., 2017).

2.6. Exemplary data: Functional wide-field imaging in Periplaneta americana

Adult cockroach males kept on a 12/12 h light/dark cycle at 24 °C and 65% humidity in the animal facility of the University of Konstanz (Konstanz, Germany) were collected, anesthetized with CO_2, and placed in a custom-built 3D-printed holder (Paoli et al., 2020; Günzel et al., 2021). Their head was restrained with soft dental wax, and a small window was opened in the head cuticle to expose the injection site. The tip of a glass capillary coated with 10 kDa dextran-conjugated Fura-2 was injected ventro-medially to the medial mushroom body calyx. After dye injection, the head capsule was closed to prevent brain desiccation. On the following day, the antennal lobe was exposed to allow optical access, and the brain was covered in transparent two-component silicon (Kwik-Sil, WPI, Sarasota, FL, USA) to limit brain movement and prevent desiccation.

Calcium imaging analysis was performed at a wide-field fluorescence microscope (BX51WI, Olympus, Tokyo, Japan) equipped with a 10x water immersion objective (Olympus UM Plan FI 10x/0.30w). Images were acquired with a SensiCam CCD camera (PCO AG, Kelheim, Germany) with a 4 × 4 binning configuration, resulting in 120 × 160 pixel-sized images. Recordings were performed at 5 frames per second using a TILLvisION acquisition system (TILL Photonics, Graefelfing, Germany). An LED system equipped with a 340 and a 385 nm LED (Omicron-Laserage Laserprodukte GmbH, Rodgau-Dudenhofen, Germany) was employed as a light source, which was directed onto the cockroach brain via a 410 short-pass filter and a 410 dichroic mirror. Emitted light was filtered through a 440 long-pass filter. Videos were exported and pre-processed in MATLAB.

Olfactory stimulation was conducted with an automatic multi-sampler for gas chromatography (Combi PAL, CTC Analytics AG, Zwingen, Switzerland). Two 1-ml odor pulses were injected at 4 and 12 s with an injection speed of 1 ml/s into a continuous flow of 1 ml/s purified air. The stimulus was directed towards the antenna via a Teflon tube (inner diameter, 0.87 mm; length, 40 cm), and the antenna was inserted into the terminal portion of the tube to ensure similar stimulation conditions across animals. An inter-trial interval of two minutes was kept between odorants, during which the syringe was flushed with clean air. At the end of a stimulation cycle, odor response to the first odorant was tested once again to assess the stability of odor responsiveness. After each set of odorants, the syringe was washed with *n*-pentane (Merk KgaA, Darmstadt, Germany), heated to 44 °C, and flushed with clean air. Each stimulation (*i.e.*, stimulus preparation, delivery, syringe flushing, *etc.*) requires approximately 3 min. For stimulation, we used butter vanillin (Dr. Oetker, Bielefeld, Germany), an extract of *Periplaneta americana* colony feces (provided by H. Nishino; Hokkaido University, Japan), and their equal mixture. Odorants were diluted to 10^{-2} in 1 ml mineral oil.

2.7. Comparison of *CalciSeg* segmentation with *k*-means clustering

A widely used approach for clustering large-scale data is *k*-means clustering (Jain, 2010; Wu et al., 2008). Yet, due to the stochastic nature of this approach, *k*-means clustering has to be run several times to achieve a satisfactory solution that approaches the optimal segmentation of the dataset. Moreover, it requires prior knowledge of the optimal number of clusters *k*, and clusters can be split into several spatially segregated regions.

The *CalciSeg* segmentation results were compared with those received via *k*-means clustering. For this, we set *k*, *i.e.*, the number of clusters to be detected by the *k*-means analysis, as the number of ROIs obtained with *CalciSeg*. Further, to obtain the best segmentation solution possible, we PCA-preprocessed the data before applying *k*-means, retaining the principal components that cumulatively account for 95% of the variance. This step reduced the third dimension of the stacks to 5.01% (bee antennal lobe), 72.50% (cockroach antennal lobe), 17.33% (locust antennal lobe glomeruli), and 8.00% (locust PN cell bodies) of the originals. We repeated the *k*-means-based segmentation 50 times, each time with a maximum number of iterations of 100. To enhance the quality of the segmentation result, we enabled an online update phase that guarantees a solution that is a local minimum of the distance criterion (squared Euclidean distance). To account for the increased processing time, we also enabled parallel processing.

In order to evaluate the variability of *k*-means clustering, we estimated the coordinates of the centroids of each pixel across repetitions and established whether it was a border pixel located between two clusters. With this information, we calculated each pixel's centroid variability (average standard deviation across repetitions) and edge variability (the proportion of times it was a border pixel: proportion of 0 = no variability, never a border pixel; 0.5 = high variability; 1 = no variability, always a border pixel).

Finally, we estimated the segmentation performance (SP; Eq. (1)) after each refinement iteration using a score that accounts for within and across cluster variability, as well as the resulting number of clusters.

$$SP = 100\frac{BCD/WCD}{\sqrt{k-1}} \quad (1)$$

with:

average between-cluster Euclidean distance, BCD; average within-cluster Euclidean distance, WCD;

number of clusters, k.

Note that clusters split into several regions were treated as different clusters and that the same minimum and maximum region size criteria as used for *CalciSeg* were applied after *k*-means clustering. This segmentation performance results in high values for well-separated clusters while penalizing increasing cluster number.

2.8. Exemplary data: Annotated ground truth datasets

To further probe the segmentation performance of *CalciSeg*, we applied it to segment publicly available motion-corrected calcium imaging datasets (Neurofinder www.neurofinder.codeneuro.org; accessed on 18-Jan-2024). This collection provides ground truth regions for the locations of individual cells. Data were pre-processed in MATLAB by resizing the images to 512 × 512 pixel followed by 2-D median filtering (3 × 3 pixel neighborhood) to account for noise and potential resizing artifacts. In addition, the temporal domain was filtered using a 3-D median filter (1 × 1 × 11 neighborhood) and resampled to 1/10 of the original size (linear interpolation of each pixel's activity time course). Eventually, the segmentation was carried out with parameters listed in Table 1. Since *CalciSeg* segments the whole image into individual granules, we identified those corresponding to active cells with distinct time-varying signals based on two criteria. First, >25% of the pixel of a granule must be active pixels, *i.e.*, pixels whose standard deviation along the temporal axis exceeds an automatic, dataset-specific threshold (multilevel image thresholds using Otsu's method applied to the standard deviation intensity projection of the dataset; five threshold values; active pixels must be above the second threshold value). The second post-segmentation criterion was that a granule had to exceed a circularity of at least 0.5 to match the shape of a cell body. The Neurofinder datasets also include labels for inactive cells, which is why we applied the same two selection criteria (minimum number of active pixels and minimum circularity) to the provided ground truth to ensure its compatibility (8.39% [5.01, 18.90] of the ground truth labels were considered active; mean, 95% confidence interval).

We evaluated the segmentation results obtained with *CalciSeg* by applying the same five metrics used by the Neurofinder benchmarking challenge to compare ground truth labels to segmentation results: recall, precision, F1 score, inclusion, and exclusion (*c.f.* www.github.com/codeneuro/neurofinder-python?tab=readme-ov-file#metrics). Recall (also known as sensitivity) describes the proportion of ground truth regions matched by the segmentation, whereas precision (also called positive predictive value) describes the proportion of segmented regions matching a ground truth label (Olson and Delen, 2008). Regions were matched in a greedy procedure (unique matches only) if the distance between the segmentation-based centroid and the ground truth centroid was below an automatic, region-specific threshold distance that is shorter for smaller regions (the major axis length of the ground truth mask). The F1 score is a combined measure of recall and precision, based on the harmonic mean of the two. Note that recall, precision, and consequently, F1 score omit the exact spatial aspects of the segmentation. To this end, we incorporated inclusion and exclusion to describe the overlap of ground truth and segmentation regions. Specifically, for each matched pair, inclusion measures the proportion of ground truth pixels, whereas exclusion measures the proportion of segmentation pixels in the intersection of the two. The final inclusion and exclusion scores are the means across all pairs.

2.9. Statistical analysis

We conducted all statistical analysis steps in MATLAB. We report averages as grand means (mean of animal means), together with bootstrapped 95% confidence intervals (with a bootstrap sample size of 5000).

2.10. Code and data availability

The MATLAB source code is available online at www.github.com/YannickGuenzel/CalciSeg/. We provide additional scripts and exemplary data at www.doi.org/10.5281/zenodo.8403062.

3. Results

3.1. Benchmark testing *CalciSeg*

The efficiency of calcium imaging data segmentation is influenced by factors such as frame size, quantity, and image complexity. The initial step of our analysis pipeline consists of compressing a calcium imaging time series into a 2-D intensity projection. This projection can be created through various mathematical operations of different complexity. Minimum and maximum projections are optimized operations that rely on the simple detection of maximum and minimum values for each pixel column. The mean projection, involving summation and division, also demonstrates a fast computational speed. On the other hand, projections like median and standard deviation exhibit higher complexity. Nevertheless, all the mentioned projection types can be processed in milliseconds to seconds on a standard commercial desktop computer (Windows 10 home; Intel® Core™ i7-7700K CPU; 32 GB memory; Samsung SSD 850 EVO). Advanced projections, such

as those using principal component analysis or correlating time vectors of individual pixels, are more computationally demanding but can still be completed within a few seconds (Fig. 1C).

A direct comparison of the projection methods revealed that — aside from the minimum projection, which tends to create a more fragmented spatial distribution with many smaller granules — all methods produce generally similar segmentation profiles (suppl. Figs. 2-5). Notably, the more computationally intensive PCA-based approach did not show any advantages over the simpler projection techniques. Furthermore, the entire *CalciSeg* processing pipeline is designed without any random elements, neither in seeding (*i.e.*, projection construction and local extremes detection) nor in the refinement process. Thus, the segmentation results are deterministic, *i.e.*, they remain unchanged across multiple runs and depend solely on the initial parameters set by the user.

To assess *CalciSeg*'s performance, we generated a mock dataset with varied image size, frame number, and image complexity (Fig. 1C–D; suppl. Fig. 1) and analyzed how these parameters influence segmentation time. The analysis showed that image size and phrase number substantially affect processing time. Image entropy, on the other hand, becomes relevant only when dealing with large stacks. In this case, processing time improves with increasing image entropy (suppl. Fig. 1), suggesting that the Voronoi tessellation and assigning pixels to a granule is faster with an increasing number of local extremes. Nevertheless, the duration of forming the intensity projection remains within the range of seconds, even when operating at a 512 × 512 pixel resolution with around a hundred granules.

To reduce processing times in view of a later refinement step, the user can select frames that are biologically relevant (such as those capturing sensory stimulation), downsample the time series by extracting frames at regular intervals, or apply PCA-based pre-processing to extract the key descriptors of the temporal dimension. All three approaches reduce the number of frames while conserving the initial signal variability. Besides frame number, inspecting how the different levels of image sizes group the processing suggests that subsampling the images by pixel binning can positively impact processing time (Fig. 1D). This can be done if allowed by the size of the structures of interest.

3.2. Segmentation of the honey bee antennal lobe glomeruli

The neuroanatomy and physiology of the honey bee antennal lobe have been extensively studied to understand the logic of olfactory coding, providing substantial knowledge of the size and location of its glomeruli. Despite proposals for computational methods for glomerular detection (Strauch et al., 2013), manual identification remains the norm in most published studies. However, with the detailed knowledge of the ground truth of glomerular anatomy, the honey bee AL provides an ideal model to assess the quality of a *CalciSeg*-based segmentation.

Distinct olfactory stimuli evoke odorant-specific patterns of glomerular responses. Thus, we can use the activity maps induced by different odorants to derive ground truth information of different response units. Analogously to combining colors in an RGB image, the average responses to three distinct odorants can be merged into a single image, facilitating the visualization of glomerular structures (Fig. 2A) and their activity (Fig. 2B). This approach allows for a direct assessment of *CalciSeg*'s segmentation accuracy by juxtaposing the size and location of glomerular activity spots in ground truth images with those derived from *CalciSeg*. Additionally, the integration of manually curated ROIs — based on our extensive knowledge of the honey bee AL — enhances this evaluation. This dual comparison offers a practical approach to test *CalciSeg*'s accuracy and to replicate expert-level segmentation.

The exemplary multiphoton data of the honey bee AL analyzed here was recorded at the modest resolution of 64 × 64 pixel but with a sampling rate of 127 frames per second. Pre-processing steps included box filtering the temporal dimension with a 21-frame filter size, and concatenating the responses to three stimuli across 369 frames each, yielding a 3-D matrix (64 × 64 × 1107; x, y, time). The segmentation was carried out based on the standard deviation-intensity projection and without additional spatial filtering. Considering the known average size of honey bee AL glomeruli (approx. 50 μm; Arnold et al. (1985)), we restricted the size of detectable granules to a range between 30 and 75 pixels, and the initial segmentation was refined for up to 100 iterations using the root median square error (Table 1). This iterative refinement process aimed to enhance the precision of the segmentation, ensuring a more accurate representation of the glomerular structures in the data. Overall, the *CalciSeg*-based segmentation yielded 77 regions with a consistent processing time of approx. 27.44 s [27.41, 27.46] (mean and 95% confidence interval).

We used the number of regions resulting from the *CalciSeg* segmentation to inform a k-means clustering-based approach (k = 77). In comparison to *CalciSeg*, k-means clustering, exhibited considerable variability in the size of the segmented regions (Fig. 2A) and with edges between regions that were inconsistent across trials (Fig. 2C). Moreover, this method produced clusters that were split into multiple regions (Fig. 2D), which contradicts the glomerular neuroanatomy. The k-means approach converges after, on average, 61 iterations (min: 37, max: 94), and the final segmentation result tends to have a lower performance score than *CalciSeg* (Fig. 2E; after accounting for split regions). The processing time of the k-means approach was shorter, with an average of approx. 1.58 s [1.44, 1.71] (mean and 95% confidence interval). Note, however, that the PCA-based pre-processing applied before k-means clustering reduced the dataset to 5.01% of its original size. Overall, even if the k-means approach is faster (neglecting the pre-processing time), the variability of its outcome and the inability to replicate the intricate details of the ground truth (Fig. 2A) underlines the reliability of *CalciSeg* over k-means clustering.

A notable limitation of k-means clustering is its dependence on prior knowledge about the number of expected regions as an initial parameter. While this could be feasible in this particular case where 28 glomeruli could be visually identified (Fig. 2A), such specificity is not always achievable, potentially inducing a strong bias in the number of detected regions. In contrast, this is not an issue for *CalciSeg*, reducing the risk of biases and making it more adaptable to various datasets. Nevertheless, its performance can be further fine-tuned by providing optional information about the minimum and maximum size of the regions of interest, if available. Taken together, this allows users to optimize the segmentation based on known anatomical details, but without being constrained by the necessity to pre-define the total number of expected regions.

3.3. Segmentation of the cockroach antennal lobe glomeruli

The antennal lobes of the American cockroach comprise approximately 200 glomeruli (Watanabe et al., 2010). Here, we re-examined a wide-field imaging dataset that was previously analyzed using an unsupervised clustering approach (Günzel et al., 2021). The overall dataset includes responses to three distinct olfactory stimuli. Each stimulus was presented twice during a single trial, and three trials were recorded per stimulus, with each of the trials lasting 80 frames. Data were captured at a spatial resolution of 160 × 120 pixels (5 frames per second; pixel size of 3.75 × 3.75 μm). Pre-processing steps included averaging repetitions to the same stimulus, cropping images to focus on the structures of interest, and concatenating the averaged responses to three stimuli, yielding a 3-D matrix (155 × 115 × 240; x, y, time). In analogy to the honey bee dataset, we generated a ground truth image by merging the average intensity projections of each stimulus into an RGB image (Fig. 2F). Given the inherent limitations of wide-field imaging, the layout of the glomeruli is less spatially resolved.

In this case, *CalciSeg* segmentation was based on the minimum-intensity projection and without additional spatial filtering. We restricted the size of detectable granules to a range between 50 and 220

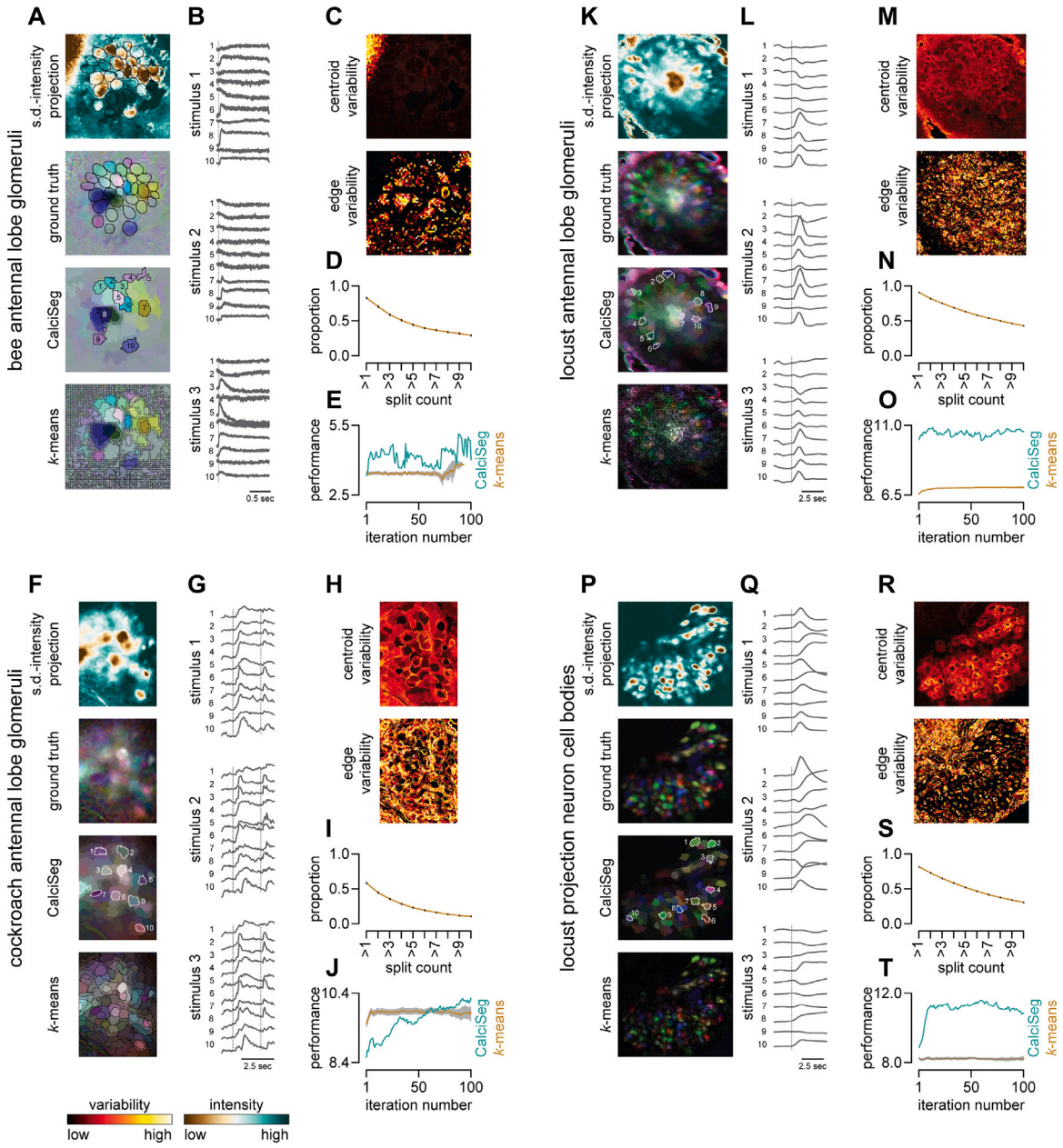

Fig. 2. *CalciSeg* outperforms *k*-means clustering on bee and cockroach datasets. **(A)** Ground truth and s.d. projection of bee antennal lobe (AL) glomeruli data segmented using *CalciSeg* and *k*-means clustering. **(B)** Time courses for ten manually selected regions based on a segmentation using *CalciSeg* (*c.f.* highlighted regions in A). **(C)** Different iterations of the *k*-means (*k* matching the number of regions obtained with *CalciSeg*) algorithm result in substantially different solutions with varying centroids (top, the average standard deviation of centroid assignment across 50 repetitions) and edges (bottom, the proportion of times a pixel was a border-pixel [0 = low, 0.5 = high, 1 = low]). **(D)** Proportion of clusters split into more than a given number of regions following a segmentation using *k*-means. **(E)** Change in segmentation performance score with an increasing number of iterations for *CalciSeg* (blue) and repeated runs of *k*-means (orange; mean with 95% confidence interval as shaded area). An early ending line indicates the reaching of a (local) optimal solution. **(F–J)** Same as A–D but for the cockroach AL glomeruli. **(K–O)** Same as A–D but for locust AL glomeruli. **(P–T)** Same as A–D but for locust projection neuron cell bodies in the AL.

pixels (based on inspecting the ground truth image), and the initial segmentation was refined for up to 100 iterations using the root median square error (Table 1). Overall, the segmentation yielded 116 regions with a consistent processing time of approx. 30.61 s [30.58, 30.65] (mean and 95% confidence interval).

The number of regions resulting from the *CalciSeg* segmentation was fed to the *k*-means clustering-based approach (k = 116). *k*-means clustering appears to segment the dataset in a comparable manner to *CalciSeg* (Fig. 2E), with some regions being sufficiently large for central pixels to be consistently assigned to the same centroid (Fig. 2H, top). Nonetheless, the exact separation along different region borders remained variable (Fig. 2H, bottom), and approximately 50% of the clusters were divided into two or more regions (Fig. 2I). The processing time of the *k*-means approach was slightly shorter than *CalciSeg*, but comparable, with an average of approx. 21.11 s [19.10, 23.08] (mean and 95% confidence interval). Also in this case, after 100 iterations, the final segmentation result based on *k*-means clustering had a lower performance score than *CalciSeg* (Fig. 2J; after accounting for split regions).

3.4. Segmentation of the locust antennal lobe microglomeruli

The locust AL presents several features that set them apart from those of other insects. Unlike other models — such as the fruit fly with

50 individually identified glomeruli (Hallem and Carlson, 2004), the honey bee with approx. 165 (Galizia et al., 1999a), or the cockroach with approx. 205 (Watanabe et al., 2010) — the locust AL houses an unusually large number of over a thousand microglomeruli (Ignell et al., 2001), that are substantially smaller (approx. 10 μm in diameter; Anton and Hansson (1996)) than, for example, a bee's glomerulus (approx. 50 μm; Arnold et al. (1985)). Moreover, all projection neurons receive input from multiple microglomeruli, unlike other insect models where the majority of PNs are uniglomerular (honey bee: Abel et al. (2001), cockroach: Paoli et al. (2020)), and individual OSNs may project to multiple glomeruli (Ignell et al., 2001). These neuroanatomical differences may have profound implications for how locusts process olfactory information and could contribute to the remarkable change from the solitarious to the gregarious phase observed across locust species. The large number of glomerular units in locusts renders hand-guided segmentation hardly feasible, underlining the importance of adopting a reliable computational approach for the study of olfactory coding in this particular insect.

Here, we analyzed the glomerular activity acquired with a confocal microscope. The dataset included responses to three olfactory stimuli of 25 frames each (five repetitions per stimulus) and was recorded at a depth of 140 μm below the AL surface with a spatial resolution of 256 × 256 pixels (pixel size of 0.77 × 0.77 μm) at 1 frame per second. Pre-processing steps included averaging repetitions to the same stimulus, cropping images to focus on the structures of interest, and concatenating the averaged responses to three stimuli, yielding a 3-D matrix (167 × 175 × 75; x, y, time). RGB data visualization of functional data (as explained above) revealed the complex glomerular organization of the locust AL (Fig. 2K).

CalciSeg segmentation was carried out based on the median-intensity projection and with additional spatial filtering. We restricted the size of detectable granules to a range between 10 and 120 pixels (based on inspecting the ground truth image), and the initial segmentation was refined for up to 100 iterations using the root median square error (Table 1). The segmentation yielded 496 regions with a consistent processing time of approx. 32.76 s [32.69, 32.82] (mean and 95% confidence interval). Altogether, *CalciSeg* managed to capture even minor functional details, accurately enveloping biological structures with distinct response patterns (Fig. 2L).

The number of regions resulting from the *CalciSeg* segmentation was used to inform k-means clustering (k = 496). In comparison to *CalciSeg*, k-means clustering produced a highly variable (Fig. 2M) and fragmented segmentation with more than 90% of the clusters being divided into two or more regions (Fig. 2N). The processing time of the k-means approach was considerably longer and more variable than *CalciSeg*, with an average of approx. 51.92 s [46.83, 54.87] (mean and 95% confidence interval). Moreover, the final segmentation result based on k-means clustering had a substantially lower performance score than *CalciSeg* (Fig. 2O; after accounting for split regions).

Taken together, this demonstrates that *CalciSeg* is particularly adept at handling complex datasets, providing an automatic and unbiased segmentation approach that outperforms traditional methods like k-means clustering.

3.5. Segmentation of the locust projection neurons' cell bodies

In many calcium imaging analysis pipelines, segmentation is primarily designed for cell bodies. Often, this encompasses preparations with genetically encoded calcium indicators, which yield bright and well-defined signals. Here, we used *CalciSeg* to segment the cell bodies of the locust AL projection neurons labeled with a dextran-conjugated calcium indicator.

As above, the dataset included responses to the three olfactory stimuli of 25 frames each (five repetitions per stimulus) recorded at a focal depth of 40 μm below the AL surface (1 frame per second, pixel size of 0.77 × 0.77 μm). Pre-processing steps comprised averaging repetitions to the same stimulus, cropping images to focus on the structures of interest, and concatenating the averaged responses to three stimuli, yielding a 3-D matrix (144 × 158 × 75; x, y, time).

CalciSeg segmentation was carried out based on the standard deviation-intensity projection and with additional spatial filtering. We restricted the size of detectable granules to a range of 30 to 120 pixels (based on inspecting the ground truth image), and the initial segmentation was refined for up to 100 iterations using the root median square error (Table 1). The segmentation yielded 307 regions with a consistent processing time of approx. 40.11 s [40.01, 40.21] (mean and 95% confidence interval).

Also in this case, the number of regions resulting from the *CalciSeg* segmentation was used to inform the k-means clustering-based approach (k = 307). In comparison to *CalciSeg*, k-means clustering appears to segment each cell into a more central and a more peripheral region (Fig. 2P). However, these separations appear to be stable across repetitions (Fig. 2R, edge variability) with merely the associated centroid changing (Fig. 2R, centroid variability). The highly fragmented nature of the k-means-based segmentation is especially apparent in the fact that more than 80% clusters were split into multiple regions (Fig. 2S). Remarkably, about one-quarter of the clusters were split into more than ten regions, which highlights a substantial challenge in achieving cohesive and biologically relevant segmentation with k-means clustering. The processing time of the k-means approach was shorter than *CalciSeg*, with an average of approx. 12.43 s [10.83, 14.11] (mean and 95% confidence interval). Note, however, that the PCA-based pre-processing applied to optimize k-means clustering reduced the dataset to 8.00% of its original size. Finally, also in this case, the segmentation performance of the k-means approach is consistently lower than that of *CalciSeg* (Fig. 2T).

Taken together, the juxtaposition of *CalciSeg*-segmented ROIs with the ground truth RGB image clearly shows its effectiveness in detecting PN somata (Fig. 2P) and extracting specific stimulus–response profiles (Fig. 2Q). This suggests that also datasets consisting of cell bodies can be easily approached with *CalciSeg* for automatic and unbiased segmentation, showcasing its potential beyond conventional cell body segmentation algorithms.

3.6. Comparison of *CalciSeg* with other segmentation methods

Common approaches for the segmentation of spatiotemporal regions rely mainly on region-growing algorithms and grouping pixels in correlation space (*e.g.*, Zhu and Yuille (1996) and Spaen et al. (2019)), or on feature extraction by using reconstruction independent component analysis (rICA, *e.g.*, Beckmann and Smith (2004), Münch et al. (2022), Aimon et al. (2019) and Weiser et al. (2023)). In order to compare *CalciSeg*-based segmentation with traditional approaches, we extended our analysis to these two methods — region-growing, and rICA — to all exemplary datasets: the honey bee, the cockroach and the locust AL data (Fig. 3; for parameters, see Table 1).

Both alternative approaches produced mixed results across the datasets. In the bee data (Fig. 3, left column), both the region-growing method and the rICA-based approach missed regions clearly identifiable in the ground truth image (white arrows). This could be explained by a generally low and homogeneous correlation space, grouping large areas to one ROI in the case of the region-growing method, or identifying the majority of pixels as a distinct region in the case of the rICA-based approach (suppl. Fig. 6 A, left column). Here, providing limits for a minimum and maximum region size aids the alternative approaches substantially, whereas an unrefined segmentation based on *CalciSeg* already provides an adequate result.

For the cockroach (Fig. 3, second column) and locust glomeruli datasets (Fig. 3, third column), the correlation-based method predominantly generated regions constrained by predefined maximum sizes. As a result, regions that were supposed to be elliptical — and segmented accordingly by *CalciSeg* — had a biologically inaccurate square shape

Table 1
Parameters for the segmentation of the different datasets using *CalciSeg* and alternative approaches. Each column represents one of the input variables. The method for calculating the projection across time (*projection_method*). The method for the initial segmentation (*init_seg_method*). The method for determining how to identify local extremes (*regmax_method*). The number of iterations for refining the granules ('n_rep'). The measure to fine-tune granule assignment (*refinement_method*). The minimum and maximum pixel area [min. max.] for each granule (*limitPixCount*). n.a. if not applicable.

dataset *approach*	projection method	init. seg. method	reg. extr. method	num. reps.	refinement method	Limit pix. count
mock data						
CalciSeg	max	Voronoi	Raw	0	rmse	[1 inf]
bee AL						
CalciSeg	mean	Voronoi	Raw	100	rmse	[30 75]
region-growing	corr	corr	Raw	0	corr	[30 75]
rICA	n.a.	rICA	Raw	0	rmse	[30 inf]
cockroach AL						
CalciSeg	min	Voronoi	Raw	100	rmse	[50 220]
region-growing	corr	corr	Raw	0	corr	[50 220]
rICA	n.a.	rICA	Raw	0	rmse	[50 inf]
locust AL glomeruli						
CalciSeg	min	Voronoi	Filtered	100	rmse	[10 120]
region-growing	corr	corr	Filtered	0	corr	[10 120]
rICA	n.a.	rICA	Filtered	0	rmse	[10 inf]
locust PN cell bodies						
CalciSeg	max	Voronoi	Filtered	100	rmse	[30 120]
region-growing	corr	corr	Filtered	0	corr	[10 120]
rICA	n.a.	rICA	Filtered	0	rmse	[10 inf]
Neurofinder datasets						
CalciSeg	max	Voronoi	Filtered	250	rmse	dataset-specific

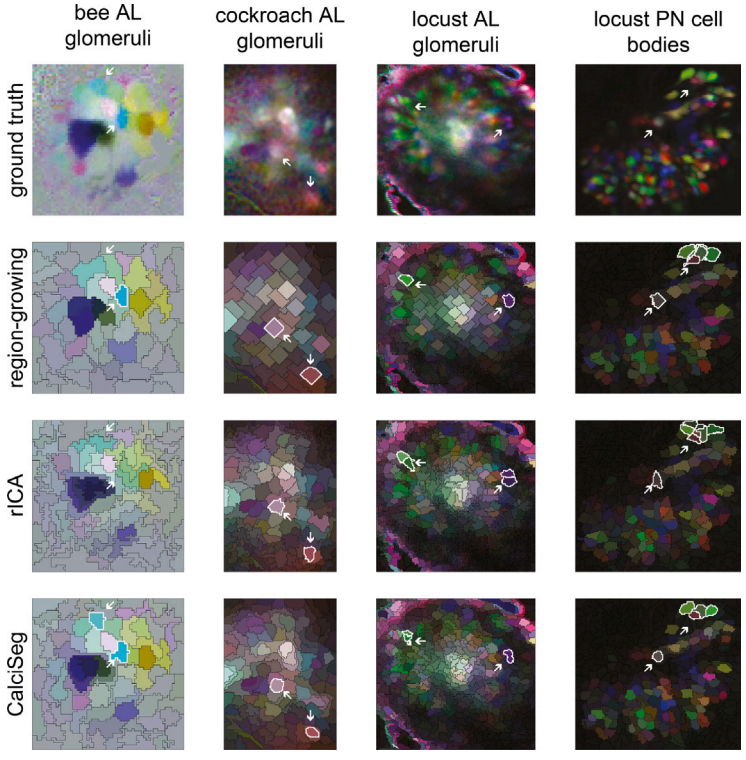

Fig. 3. Comparison of a *CalciSeg*-based segmentation with a correlation-based region-growing and an independent component analysis approach. We evaluated the segmentation of different datasets (columns) based on the ground truth RGB image. We show a segmentation with a correlation-based region-growing approach (second row) that gradually increases a region based on the dataset's correlation space until a threshold or a maximum region size has been reached. Further, we employed a segmentation based on reconstruction independent component analysis (third row) that extracts distinct features from the data. Both approaches were compared with the *CalciSeg*-based segmentation from Fig. 2 (last row). White arrowheads and outlined regions highlight the differences between the different approaches. See Table 1 for input parameters.

(white arrows). Notably, while some regions were segmented similarly by all three methods (*e.g.*, locust glomeruli data, white arrows), *CalciSeg* uniquely captured more delicate details aligned with the ground truth image.

Last, for locust PN cell body data (Fig. 3, right column), all three approaches produced comparable segmentation results. Yet, only *CalciSeg* managed to a precise identification of challenging regions (white arrows). Note that this could be achieved also with the region-growing or rICA-based approaches when additional refinement steps were added (suppl. Fig. 6D, right column). However, already the raw *CalciSeg*-based segmentation included these regions (suppl. Fig. 6D, left column). Taken together, *CalciSeg* offers a more efficient and anatomically accurate segmentation, especially for datasets where biological structures are complex and vary in both shape and size.

3.7. Segmentation of sparsely distributed cells

Extracting regions that correspond to individual neurons remains a major challenge in functional imaging analysis. For this reason, projects like Neurofinder (www.neurofinder.codeneuro.org/) provide collections of datasets with ground truth labels. These datasets can be used to benchmark test algorithms that aim for an automatic detection of cells in time-varying images. Here, we used the provided labels — which were manually curated and also contained neurons that were not active — to test the quality of *CalciSeg* segmentation on such a dataset (Fig. 4A).

To evaluate how well ground truth labels are matched by *CalciSeg*-found granules, we calculated standard segmentation scores as metrics (Fig. 4B). Despite the rigid nature of simple threshold criteria used to identify active cells (see Methods for details), *CalciSeg* reached strong F1 (0.68 [0.58, 0.77]; mean, 95% confidence interval), recall (0.92 [0.87, 0.96]), precision (0.59 [0.47, 0.69]), inclusion (0.67 [0.60, 0.72]), and exclusion (0.83 [0.79, 0.86]) scores. Taken together, these findings suggest that *CalciSeg* segmentation of sparsely distributed cells with varying levels of activity closely matches manually curated ground truth labels, underlining *CalciSeg*'s utility in sophisticated neuronal segmentation tasks.

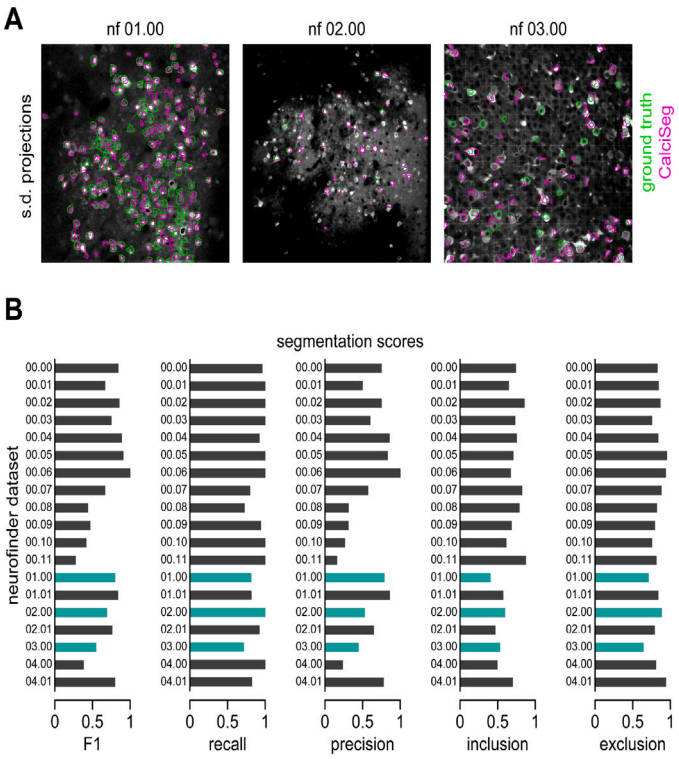

Fig. 4. Segmentation scores for *CalciSeg* on the Neurofinder datasets. **(A)** Three exemplary Neurofinder datasets are shown as standard deviation-intensity projections with superimposed locations of active cells based on ground truth labels (green) and matching *CalciSeg* granules (magenta). **(B)** Cell segmentation score metrics for all 19 Neurofinder datasets with examples from A highlighted in blue. Higher scores indicate better performances for each metric (see Methods for details).

4. Discussion

The significant improvements in spatiotemporal resolution and light sensitivity in optical microscopy, along with the increased reporting fidelity of fluorescent functional indicators, have made calcium imaging a prominent method in neuroscience. Notably, functional imaging provides the intrinsic advantage of simultaneous tracking of all functional units within the field of view, being them synapses, cell bodies, or entire neuropils. The wide adoption of calcium imaging analysis stimulated the requirement for and development of analytical tools capable of automatically detecting regions of interest (ROIs) in an unbiased, unsupervised, and reproducible manner. Still, while the reliable extraction of spatial and temporal coherence is fundamental for high-quality mapping of neuronal dynamics *in vivo*, the complexity and diversity of datasets render a unified approach challenging.

Here, we present *CalciSeg*, a segmentation method based on Voronoi tessellation followed by iterative refinements of the size and shape of the detected functional regions (Fig. 1A–B). *CalciSeg* segmentation is unbiased and unsupervised. As such, it can enable efficient ROI detection without any *a priori* information, *e.g.*, on the quantity or size of the structures to be segmented and does not require a training dataset. Nevertheless, the algorithm's efficiency can be further enhanced by providing the expected size range of the target functional regions (biologically relevant information that the user generally knows).

CalciSeg image segmentation begins by detecting seeds that are deterministically defined as local extremes in the time-collapsed 2-D intensity projection of a functional imaging recording. Within the projection, each pixel is automatically assigned to its closest seed, and in an iterative process, intermediate pixels are assigned to adjacent segmented regions based on time-trace similarity. In other words, a pixel is assigned to the neighboring ROI with the most similar temporal dynamics. Since none of these processes involve stochastic components but rely solely on deterministic mathematical operations, the resulting segmentation is reproducible across trials and does not benefit from (nor require) optimization through multiple replications.

Segmentation speed is a function of image size, frame number, and image complexity (Fig. 1C–D, suppl. Fig. 1B-C). Image size can be reduced by pixel binning (if allowed by the dimension of the regions to be segmented relatively to the acquired resolution). Similarly, an unsupervised video sub-sampling or a supervised selection of biologically relevant frames can be a practical approach to reduce frame number with limited loss of relevant information. Image complexity is an intrinsic property of the biological sample and cannot (nor should) be modified. Overall, *CalciSeg* processing speed on a commercial desktop computer remains in the order of seconds even for realistically large datasets (*e.g.*, 512-by-512 pixels over 1000 frames). Fast processing times are crucial for online analysis and feature detection during ongoing experiments, rendering *CalciSeg* a valuable addition to existing analysis pipelines.

CalciSeg segmentation approach was challenged with functional imaging data from biological specimens with different ROI sizes and numbers. Notably, we demonstrated that *CalciSeg* can successfully and reliably detect olfactory glomerular structures in three different insect models — *i.e.*, *A. mellifera*, *P. americana*, and *S. gregaria* - with glomerular diameters ranging from approx. 50 μm in bees (Arnold et al., 1985) to 10 μm in the locust (Anton and Hansson, 1996). Furthermore, *CalciSeg* efficiency was challenged to segment individual cell bodies, both tightly packed (olfactory projection neurons in the locust antennal

lobe) and sparsely distributed (Neurofinder datasets; www.neurofinder.codeneuro.org). In both cases, it could correctly detect the cell bodies, closely matching manual labeling reliability (Figs. 3 and 4).

The Neurofinder datasets pose a valuable challenge for automatic calcium imaging segmentation approaches as the provided images are heterogeneous and vary strongly in brightness with imbalanced and sometimes inconsistent ground truth labels (discussed in Klibisz et al. (2017)). Common automatic calcium imaging segmentation algorithms like HNCcorr (Spaen et al., 2019), UNet2DS (Klibisz et al., 2017), or Suite2p (Pachitariu et al., 2016) reach F1 scores ranging from approx. 0.5 to 0.6 (see Tbl. 1 in Klibisz et al. (2017) for details) for the automatic detection of cells. Introducing simple criteria for automatically selecting active cells based on pixel variance and region circularity, our approach detected efficiently the ground truth locations, reaching comparable segmentation scores (mean F1: 0.68, Fig. 4). Together with high inclusion (0.67) and exclusion (0.83) values — describing the spatial overlap of the segmented regions with the ground truth labels — this evaluation further corroborates the effectiveness of *CacliSeg*.

All in all, *CalciSeg* provides a versatile segmentation tool for different specimens with varied ROI structures. This provides an advantage over alternative solutions designed to solve more specific tasks, which are less flexible in detecting biological structures of higher variability. For instance, KNIME (Strauch et al., 2013) was optimized for the detection of olfactory glomeruli, whereas other studies have implemented custom solutions (*e.g.*, ICA in Münch et al. (2022) for gustatory processing regions in the ventral fly brain) for novel segmentation problems. On the other hand, CaImAn — recognized as one of the most complete pipelines for calcium imaging analysis — has been designed to segment cellular structures (Giovannucci et al., 2019). As such, it has been applied essentially for cell body detection and is less suitable for neuropils of different sizes and shapes.

Finally, we assessed *CalciSeg* segmentation efficiency and efficacy compared to alternative approaches based on region-growing algorithms, *k*-means clustering, and feature extraction (*e.g.*, rICA). Across the different datasets containing structures varying in shape and size, *CalciSeg* consistently produced results closely aligning with the ground truth images, thus providing more anatomically accurate segmentation results (Figs. 2 and 3). In the honey bee antennal lobe glomeruli dataset, for example, *CalciSeg* not only avoided overly fragmented results as seen with *k*-means clustering — adhering more closely to the known neuroanatomy — but also outperformed rICA and the region-growing approach, which failed to identify less conspicuous regions. Furthermore, unlike *k*-means clustering, which often results in inconsistent region sizes and shapes, *CalciSeg* does not require *a priori* knowledge of the number of regions, offering a deterministic and unbiased approach that produces consistent results across multiple runs, without the need for preliminary data reduction, such as PCA pre-processing employed before *k*-means to manage data size and complexity.

In summary, *CalciSeg* provides a readily accessible package (www.github.com/YannickGuenzel/CalciSeg/) designed to conduct functional imaging analysis segmentation across multiple scales effectively. Recent advances in functional imaging techniques for non-transgenic insect models (Skiri et al., 2004; Mertes et al., 2021; Paoli et al., 2020; Petelski et al., 2024) and improvements in spatial and temporal resolution during data acquisition pose exciting challenges for image segmentation and signal source extraction tools. With the increasing complexity of calcium imaging datasets, the need for suitable tools becomes paramount to enhance the interpretability and reproducibility of functional imaging analysis. Yet, segmentation approaches that require tuning of a multitude of parameters or an extensive and representative training dataset remain difficult to implement and integrate into existing analysis pipelines. Altogether, *CalciSeg* offers an efficient segmentation method that is well-suited for integration into real-time imaging workflows with varied data acquisition configurations and different biological specimens.

CRediT authorship contribution statement

Yannick Günzel: Writing – review & editing, Writing – original draft, Visualization, Software, Formal analysis, Conceptualization. **Einat Couzin-Fuchs:** Writing – review & editing, Writing – original draft, Supervision, Project administration, Funding acquisition. **Marco Paoli:** Writing – review & editing, Writing – original draft, Supervision, Project administration, Conceptualization.

Declaration of competing interest

The authors declare no competing interests.

Data availability

The MATLAB source code is available online at www.github.com/YannickGuenzel/CalciSeg/. We provide additional scripts and exemplary data at www.doi.org/10.5281/zenodo.8403062.

Acknowledgments

This work was completed with the support of the Deutsche Forschungsgemeinschaft (DFG, German Research Foundation) under Germany's Excellence Strategy – EXC 2117 – 422037984.

Ethics statement

This study was carried out in accordance with the recommendations of the "3Rs" principles as stated in the Directive 2010/63/EU and all procedures were performed following the guidelines of the German animal welfare law.

Appendix A. Supplementary data

Supplementary material related to this article can be found online at https://doi.org/10.1016/j.neuroimage.2024.120758.

References

Abbas, W., Masip, D., 2022. Computational methods for neuron segmentation in two-photon calcium imaging data: A survey. Appl. Sci. 12 (14), 6876.
Abel, R., Rybak, J., Menzel, R., 2001. Structure and response patterns of olfactory interneurons in the honeybee, Apis mellifera. J. Comp. Neurol. 437 (3), 363–383.
Ahrens, M.B., Orger, M.B., Robson, D.N., Li, J.M., Keller, P.J., 2013. Whole-brain functional imaging at cellular resolution using light-sheet microscopy. Nat. Methods 10 (5), 413–420.
Aimon, S., Katsuki, T., Jia, T., Grosenick, L., Broxton, M., Deisseroth, K., Sejnowski, T.J., Greenspan, R.J., 2019. Fast near-whole–brain imaging in adult Drosophila during responses to stimuli and behavior. PLoS Biol. 17 (2), e2006732.
Anton, S., Hansson, B.S., 1996. Antennal lobe interneurons in the desert locust Schistocerca gregaria (Forskal): processing of aggregation pheromones in adult males and females. J. Comp. Neurol. 370 (1), 85–96.
Arnold, G., Masson, C., Budharugsa, S., 1985. Comparative study of the antennal lobes and their afferent pathway in the worker bee and the drone (Apis mellifera). Cell Tissue Res. 242, 593–605.
Beckmann, C.F., Smith, S.M., 2004. Probabilistic independent component analysis for functional magnetic resonance imaging. IEEE Trans. Med. Imaging 23 (2), 137–152.
Bestea, L., Paoli, M., Arrufat, P., Ronsin, B., Carcaud, J., Sandoz, J.-C., Velarde, R., Giurfa, M., de Brito Sanchez, M.G., 2022. The short neuropeptide F regulates appetitive but not aversive responsiveness in a social insect. Iscience 25 (1).
Bilz, F., Geurten, B.R., Hancock, C.E., Widmann, A., Fiala, A., 2020. Visualization of a distributed synaptic memory code in the Drosophila brain. Neuron 106 (6), 963–976.
Chen, T.-W., Wardill, T.J., Sun, Y., Pulver, S.R., Renninger, S.L., Baohan, A., Schreiter, E.R., Kerr, R.A., Orger, M.B., Jayaraman, V., et al., 2013. Ultrasensitive fluorescent proteins for imaging neuronal activity. Nature 499 (7458), 295–300.
Denk, W., Yuste, R., Svoboda, K., Tank, D.W., 1996. Imaging calcium dynamics in dendritic spines. Curr. Opin. Neurobiol. 6 (3), 372–378.
Galizia, C.G., McIlwrath, S.L., Menzel, R., 1999a. A digital three-dimensional atlas of the honeybee antennal lobe based on optical sections acquired by confocal microscopy. Cell Tissue Res. 295, 383–394.

Galizia, C.G., Sachse, S., Rappert, A., Menzel, R., 1999b. The glomerular code for odor representation is species specific in the honeybee apis mellifera. Nat. Neurosci. 2 (5), 473–478.
Giovannucci, A., Friedrich, J., Gunn, P., Kalfon, J., Brown, B.L., Koay, S.A., Taxidis, J., Najafi, F., Gauthier, J.L., Zhou, P., et al., 2019. CaImAn an open source tool for scalable calcium imaging data analysis. elife 8, e38173.
Günzel, Y., McCollum, J., Paoli, M., Galizia, C.G., Petelski, I., Couzin-Fuchs, E., 2021. Social modulation of individual preferences in cockroaches. Iscience 24 (1).
Hallem, E.A., Carlson, J.R., 2004. The odor coding system of Drosophila. TRENDS Genet. 20 (9), 453–459.
Hansson, B., Ochieng', S., Grosmaitre, X., Anton, S., Njagi, P., 1996. Physiological responses and central nervous projections of antennal olfactory receptor neurons in the adult desert locust, Schistocerca gregaria (Orthoptera: Acrididae). J. Comp. Physiol. A 179, 157–167.
Hires, S.A., Tian, L., Looger, L.L., 2008. Reporting neural activity with genetically encoded calcium indicators. Brain Cell Biol. 36, 69–86.
Ignell, R., Anton, S., Hansson, B.S., 2001. The antennal lobe of Orthoptera–anatomy and evolution. Brain Behav. Evol. 57 (1), 1–17.
Islam, M.S., Suryavanshi, P., Baule, S.M., Glykys, J., Baek, S., 2023. A deep learning approach for neuronal cell body segmentation in neurons expressing GCaMP using a swin transformer. Eneuro 10 (9).
Jain, A.K., 2010. Data clustering: 50 years beyond K-means. Pattern Recognit. Lett. 31 (8), 651–666.
Jayaraman, V., Laurent, G., 2007. Evaluating a genetically encoded optical sensor of neural activity using electrophysiology in intact adult fruit flies. Front. Neural Circuits 1, 74.
Kerr, J.N., Denk, W., 2008. Imaging in vivo: watching the brain in action. Nat. Rev. Neurosci. 9 (3), 195–205.
Klibisz, A., Rose, D., Eicholtz, M., Blundon, J., Zakharenko, S., 2017. Fast, simple calcium imaging segmentation with fully convolutional networks. In: International Workshop on Deep Learning in Medical Image Analysis. Springer, pp. 285–293.
Mertes, M., Carcaud, J., Sandoz, J.-C., 2021. Olfactory coding in the antennal lobe of the bumble bee bombus terrestris. Sci. Rep. 11 (1), 10947.
Miyawaki, A., Llopis, J., Heim, R., McCaffery, J.M., Adams, J.A., Ikura, M., Tsien, R.Y., 1997. Fluorescent indicators for Ca2+ based on green fluorescent proteins and calmodulin. Nature 388 (6645), 882–887.
Mölter, J., Avitan, L., Goodhill, G.J., 2018. Detecting neural assemblies in calcium imaging data. BMC Biol. 16 (1), 1–20.
Mukamel, E.A., Nimmerjahn, A., Schnitzer, M.J., 2009. Automated analysis of cellular signals from large-scale calcium imaging data. Neuron 63 (6), 747–760.
Münch, D., Goldschmidt, D., Ribeiro, C., 2022. The neuronal logic of how internal states control food choice. Nature 607 (7920), 747–755.
Olson, D.L., Delen, D., 2008. Advanced Data Mining Techniques. Springer Science & Business Media.
Otsu, N., 1979. A threshold selection method from gray-level histograms. IEEE Trans. Syst. Man Cybern. 9 (1), 62–66.
Pachitariu, M., Stringer, C., Schröder, S., Dipoppa, M., Rossi, L.F., Carandini, M., Harris, K.D., 2016. Suite2p: beyond 10,000 neurons with standard two-photon microscopy. 061507, BioRxiv.
Paoli, M., Andrione, M., Haase, A., 2017. Imaging techniques in insects. In: Lateralized Brain Functions. Springer, pp. 471–519.
Paoli, M., Nishino, H., Couzin-Fuchs, E., Galizia, C.G., 2020. Coding of odour and space in the hemimetabolous insect Periplaneta americana. J. Exp. Biol. 223 (3), jeb218032.
Paoli, M., Wystrach, A., Ronsin, B., Giurfa, M., 2024. Smell and aftersmell: Fast calcium imaging dynamics of honey bee olfactory coding. eLife 13.
Petelski, I., Günzel, Y., Sayin, S., Kraus, S., Couzin-Fuchs, E., 2024. Synergistic olfactory processing for social plasticity in desert locusts. Nature Commun. 15 (1), 5476.
Pnevmatikakis, E.A., 2019. Analysis pipelines for calcium imaging data. Curr. Opin. Neurobiol. 55, 15–21.
Raiser, G., Galizia, C.G., Szyszka, P., 2017. A high-bandwidth dual-channel olfactory stimulator for studying temporal sensitivity of olfactory processing. Chem. Senses 42 (2), 141–151.
Reidl, J., Starke, J., Omer, D.B., Grinvald, A., Spors, H., 2007. Independent component analysis of high-resolution imaging data identifies distinct functional domains. Neuroimage 34 (1), 94–108.
Sachse, S., Galizia, C.G., 2002. Role of inhibition for temporal and spatial odor representation in olfactory output neurons: a calcium imaging study. J. Neurophysiol. 87 (2), 1106–1117.
Sachse, S., Galizia, C.G., 2003. The coding of odour-intensity in the honeybee antennal lobe: local computation optimizes odour representation. Eur. J. Neurosci. 18 (8), 2119–2132.
Sachse, S., Rappert, A., Galizia, C.G., 1999. The spatial representation of chemical structures in the antennal lobe of honeybees: steps towards the olfactory code. Eur. J. Neurosci. 11 (11), 3970–3982.
Sità, L., Brondi, M., Lagomarsino de Leon Roig, P., Curreli, S., Panniello, M., Vecchia, D., Fellin, T., 2022. A deep-learning approach for online cell identification and trace extraction in functional two-photon calcium imaging. Nature Commun. 13 (1), 1529.
Skiri, H.T., Galizia, C.G., Mustaparta, H., 2004. Representation of primary plant odorants in the antennal lobe of the moth Heliothis virescens using calcium imaging. Chem. Senses 29 (3), 253–267.
Soelter, J., Schumacher, J., Spors, H., Schmuker, M., 2014. Automatic segmentation of odor maps in the mouse olfactory bulb using regularized non-negative matrix factorization. NeuroImage 98, 279–288.
Spaen, Q., Asín-Achá, R., Chettih, S.N., Minderer, M., Harvey, C., Hochbaum, D.S., 2019. HNCcorr: A novel combinatorial approach for cell identification in calcium-imaging movies. eneuro 6 (2).
Spruit, H.C., Nordlund, A., Title, A., 1990. Solar convection. Annu. Rev. Astron. Astrophys. 28 (1), 263–303.
Strauch, M., Galizia, C.G., 2011. Fast PCA for processing calcium-imaging data from the brain of Drosophila melanogaster. In: Proceedings of the ACM Fifth International Workshop on Data and Text Mining in Biomedical Informatics. pp. 3–10.
Strauch, M., Rein, J., Lutz, C., Galizia, C.G., 2013. Signal extraction from movies of honeybee brain activity: the ImageBee plugin for KNIME. BMC Bioinform. 14, 1–13.
Stringer, C., Wang, T., Michaelos, M., Pachitariu, M., 2021. Cellpose: a generalist algorithm for cellular segmentation. Nat. Methods 18 (1), 100–106.
Tsien, R.Y., 1980. New calcium indicators and buffers with high selectivity against magnesium and protons: design, synthesis, and properties of prototype structures. Biochemistry 19 (11), 2396–2404.
Varoquaux, G., Sadaghiani, S., Pinel, P., Kleinschmidt, A., Poline, J.-B., Thirion, B., 2010. A group model for stable multi-subject ICA on fMRI datasets. Neuroimage 51 (1), 288–299.
Watanabe, H., Nishino, H., Nishikawa, M., Mizunami, M., Yokohari, F., 2010. Complete mapping of glomeruli based on sensory nerve branching pattern in the primary olfactory center of the cockroach periplaneta americana. J. Comp. Neurol. 518 (19), 3907–3930.
Weiser, S.C., Mullen, B.R., Ascencio, D., Ackman, J.B., 2023. Data-driven segmentation of cortical calcium dynamics. PLoS Comput. Biol. 19 (5), e1011085.
Wilson, R.I., Mainen, Z.F., 2006. Early events in olfactory processing. Annu. Rev. Neurosci. 29, 163–201.
Wirtshafter, H.S., Disterhoft, J.F., 2022. In vivo multi-day calcium imaging of CA1 hippocampus in freely moving rats reveals a high preponderance of place cells with consistent place fields. J. Neurosci. 42 (22), 4538–4554.
Wu, X., Kumar, V., Ross Quinlan, J., Ghosh, J., Yang, Q., Motoda, H., McLachlan, G.J., Ng, A., Liu, B., Yu, P.S., et al., 2008. Top 10 algorithms in data mining. Knowl. Inf. Syst. 14, 1–37.
Zhu, S.C., Yuille, A., 1996. Region competition: Unifying snakes, region growing, and Bayes/MDL for multiband image segmentation. IEEE Trans. Pattern Anal. Mach. Intell. 18 (9), 884–900.